



This is a repository copy of *Adaptive chaotic particle swarm algorithm for isogeometric multi-objective size optimization of FG plates*.

White Rose Research Online URL for this paper:  
<http://eprints.whiterose.ac.uk/158859/>

Version: Accepted Version

---

**Article:**

Wang, C., Yu, T., Curiel-Sosa, J.L. [orcid.org/0000-0003-4437-1439](https://orcid.org/0000-0003-4437-1439) et al. (2 more authors) (2019) Adaptive chaotic particle swarm algorithm for isogeometric multi-objective size optimization of FG plates. *Structural and Multidisciplinary Optimization*, 60 (2). pp. 757-778. ISSN 1615-147X

<https://doi.org/10.1007/s00158-019-02238-2>

---

This is a post-peer-review, pre-copyedit version of an article published in *Structural and Multidisciplinary Optimization*. The final authenticated version is available online at:  
<https://doi.org/10.1007/s00158-019-02238-2>

**Reuse**

Items deposited in White Rose Research Online are protected by copyright, with all rights reserved unless indicated otherwise. They may be downloaded and/or printed for private study, or other acts as permitted by national copyright laws. The publisher or other rights holders may allow further reproduction and re-use of the full text version. This is indicated by the licence information on the White Rose Research Online record for the item.

**Takedown**

If you consider content in White Rose Research Online to be in breach of UK law, please notify us by emailing [eprints@whiterose.ac.uk](mailto:eprints@whiterose.ac.uk) including the URL of the record and the reason for the withdrawal request.



[eprints@whiterose.ac.uk](mailto:eprints@whiterose.ac.uk)  
<https://eprints.whiterose.ac.uk/>

# Adaptive chaotic particle swarm algorithm for isogeometric multi-objective size optimization of FG plates

Chao Wang<sup>1,2</sup> · Tiantang Yu<sup>1</sup> · Jose L. Curiel-Sosa<sup>3</sup> · Nenggang Xie<sup>2</sup> · Tinh Quoc Bui<sup>4,5</sup>

## Abstract

An effective multi-objective optimization methodology that combines the isogeometric analysis (IGA) and adaptive chaotic particle swarm algorithm is presented for optimizing ceramic volume fraction (CVF) distribution of functionally graded plates (FGPs) under eigenfrequencies. The CVF distribution is represented by the B-spline basis function. Mechanical behaviors of FGPs are obtained with NURBS-based IGA and the recently developed simple first-order shear theory. The design variables are the CVFs at control points in the thickness direction, and the optimization objective is to minimize the mass of structure and maximize the first natural frequency. A recently developed multi-objective adaptive chaotic particle swarm algorithm with high efficiency is employed as an optimizer. All desirable features of the developed approach will be illustrated through four numerical examples, confirming its effectiveness and reliability.

**Keywords** Functionally graded plates · Material distribution · Multi-objective optimization · IGA · Free vibration · Adaptive chaos particle swarm algorithm

## 1 Introduction

Material properties of functionally graded plates (FGPs) vary continuously and smoothly through the plate thickness; thus, the delamination problems which often exist in the conventional layered composites could be eliminated. Owing to the outstanding mechanical features, FGPs have been extensively

used in many engineering fields including civil, mechanical, aeronautical, and marine. The ceramic-metal FGP is one typical FGP, and its volume fraction distribution is often described with a mathematical function with gradient factors such as the power function (Moita et al. 2018), exponential function (Woodward and Kashtalyan 2011), trigonometric function (Magnucka-Blandzi 2011), and polynomial function (Nair et al. 2006). The desired material properties can be achieved by changing the gradient factors. In order to consider individual properties of practical problems and meet the desired implementation, it is necessary to determine the optimal volume fraction distribution in a FGP under certain constraints. In the foregoing work of optimizing the volume fraction distribution, which is also known as size optimization, the parameters of the distribution function are often taken as variables, and the objective function is defined according to the working conditions; the optimal volume fraction distribution can be obtained using an optimization method (Na and Kim 2009; Roque et al. 2016; Daynes et al. 2017; Shi and Shimoda 2015; Kou et al. 2012). The optimization result depends on the selected distribution function; thus, this approach limits the material variability (Lieu and Lee 2017; Lieu et al. 2018). Hence, it is necessary to develop a new means which can create complex and smooth material profiles with least possible numbers of design variables (Taheri and Hassani 2014).

---

✉ Tiantang Yu  
tiantangyu@hhu.edu.cn

✉ Tinh Quoc Bui  
buiquoctinh@duytan.edu.vn; bui.t.aa@m.titech.ac.jp

<sup>1</sup> Department of Engineering Mechanics, Hohai University, Nanjing 211100, People's Republic of China

<sup>2</sup> Department of Mechanical Engineering, Anhui University of Technology, Ma'anshan, People's Republic of China

<sup>3</sup> Department of Mechanical Engineering, University of Sheffield, Sir Frederik Mappin, Mappin St, Sheffield, UK

<sup>4</sup> Institute for Research and Development, Duy Tan University, Da Nang City, Vietnam

<sup>5</sup> Department of Civil and Environmental Engineering, Tokyo Institute of Technology, 2-12-1-W8-22, Ookayama, Meguro-ku, Tokyo 152-8552, Japan

Isogeometric analysis (IGA) (Hughes et al. 2005) takes CAD spline functions (e.g., NURBS) as the shape functions of finite element analysis; it thus shows many good properties such as the exact computational geometry, simple mesh refinement, higher-order continuity, and without the aid of conventional mesh generators. The IGA has been used to solve a large number of engineering problems (see, e.g., (Fantuzzi and Tomabene 2016; Lezgy-Nazargah et al. 2015; Klinkel et al. 2015; Farzam-Rad et al. 2017; Yu et al. 2015, 2016a, b, 2017; Liu et al. 2017a, b; Lai et al. 2017; Sun et al. 2018) and references therein). Recently, several researchers studied the volume fraction distribution of FG structures using IGA. Optimizing eigenfrequencies of FG structures using a full IGA for the simultaneous material composition and shape design was analyzed by Taheri and Hassani (Taheri and Hassani 2014). The graded material distributions are captured using the parameterization based on the NURBS functions. The in-plane coordinates of control points which define the design boundary surfaces and the vertical coordinates of all control points which describe the variations of material properties are considered as design variables. The obtained results are much better dynamic performance compared with the optimal results of the simple shape or material composition design. Taheri et al. (Taheri et al. 2014) used B-spline basis functions to construct volume fraction distribution of FG structures for thermo-mechanical optimization under the framework of IGA. An effective numerical optimization method for ceramic volume fraction (CVF) distribution of FGPs in the thermo-mechanical environment was proposed by Lieu and Lee (Lieu and Lee 2017). The material distribution is described with control points along the plate thickness using the B-spline basis functions. An IGA model based on NURBS and the third-order shear deformation plate theory was developed for calculating static response of the FGPs, and an adaptive hybrid evolutionary firefly algorithm was employed to solve compliance minimization problems with volume constraints. Later, Lieu et al. (Lieu et al. 2018) used the same method to optimize the CVF distribution and layer thicknesses of the functional sandwich plates under eigenfrequencies. The single objective is often used in the above optimization. The optimization objective may be the stress minimization (Taheri et al. 2014), the mass minimization (Taheri and Hassani 2014), or the first natural frequency minimization (Lieu and Lee 2017; Lieu et al. 2018). In engineering applications, the multi-objective optimization however is often required; for example, we need to minimize the stress and the mass for the FGPs used in the aeronautical structure.

In this study, the multi-objective size optimization of FGPs is performed based on the IGA. The CVFs at control points along the thickness of plates are utilized to represent material distribution via the B-spline functions. Owing to the high-order continuity of B-spline functions, the material properties

along the thickness direction vary continuously and smoothly. The B-spline functions are always positive, so the interpolated volume fraction at one point always strictly satisfies the constraint between 0 and 1 without any additional conditions. Kirchhoff theory and first-order shear deformation theory (FSDT) are two widely accepted plate theories. While the Kirchhoff theory (Liew et al. 2011) is suitable for thin plates only, the FSDT (Reissner 1976), on the contrary, captures well the shear deformation effects for thick plates. One downside of the conventional FSDT is the shear-locking issue once dealing with thin plates. Recently, a simple first-order shear theory (S-FSDT) (see, e.g., (Yu et al. 2015, 2016b; Vu et al. 2017) and references therein) was developed, with its key idea is to decompose the transverse displacement into bending part and shear part, and express the rotations with the partial derivatives of the transverse bending displacement. Compared with the conventional FSDT, the S-FSDT inherently owns some superior features: (1) free from shear locking, (2) capturing the shear deformation effect, and (3) less one unknown. Although the  $C^1$ -continuity is required in the S-FSDT, it is automatically satisfied thanks to the higher-order continuity feature of the IGA. This issue was already addressed in (Yu et al. 2015; Liu et al. 2017a; Yin et al. 2014), where the IGA associated with the S-FSDT was used to study the mechanical behaviors of FGPs.

Multi-objective evolutionary algorithms (Schaffer 1985) can provide multiple optimal solution sets; thus, decision-makers can select the final scheme according to their own needs. At present, multi-objective evolutionary algorithms have become a major means to solve the multi-objective optimization problem. The multi-objective evolutionary algorithms are generally developed based on the swarm intelligence algorithm. Compared with the traditional method of moving asymptote (MMA) (Svanberg 1987), although evolutionary algorithms will spend more computation time, the evolutionary algorithm has two key advantages: (1) it does not need the derivation of complex partial derivatives and (2) the optimization process can be closed-loop adjusted by the objective value in each iteration. In this way, the optimal results are less affected by initial values. There are many multi-objective evolutionary algorithms so far, such as the non-dominated sorting genetic algorithm (NSGA) (Deb et al. 2002; Srinivas and Deb 1994), the multi-objective particle swarm optimization algorithm (MOPSO) (Coello and Lechuga 2002), the multi-objective artificial bee colony algorithm (MOABC) (Akbari et al. 2012), the multi-objective differential evolution (MODE) (Zakaria et al. 2014), the multi-objective immune system algorithm (MOIS) (Coello and Cortes 2002), the multi-objective group search optimizer (MOGSO) (Wang et al. 2012), and the multi-objective game theory (MOGT) (Wang et al. 2010; Xie et al. 2013). The MOPSO algorithm is one of the most effective multi-objective evolutionary algorithms and it has been applied to

a wide range of fields (Qasem and Shamsuddin 2011; Briza and Naval 2010; Kulkarni et al. 2015). The MOPSO algorithm is thus adopted for the analysis in this study. Alatas and Akin (2009) developed a multi-objective chaotic particle swarm optimization (MOCPSO) algorithm as a search strategy to mine classification rules within datasets, and chaotic sequence was introduced to obtain particle diversity. In order to further improve the efficiency of optimization, we develop the MOCPSO algorithm in the sense that takes into account the following issues: (1) the adaptive strategy is proposed for fitness selection to take account of the optimization process of the algorithm and (2) some directional perturbation mechanisms of elite solutions are added to expand the coverage of the Pareto frontier. We name this revised method as multi-objective adaptive chaotic particle swarm optimization algorithm (MOACPSO).

In engineering application, it is an urgent problem to find a reasonable material distribution for any shape of functionally graded plates, considering different working conditions and requirements. This paper aims to address the scientific question and the specific measures. Firstly, the IGA in association with S-FSDT, which serves as a high-precision numerical algorithm, is employed to analyze the mechanical problems of functionally graded plates. Secondly, the multi-objective evolutionary algorithm is used in the effective optimization technique, so that the decision-maker can select the final optimization scheme of functional gradient board according to his own needs. The major motivation of the present paper is to develop the size optimization of arbitrary shape FGPs by using IGA in combination with multi-objective evolutionary algorithm which is rather rare in the literature. In addition, B-spline basic function is used to replace the traditional function to describe material distribution, under which the corresponding control points are taken as design variables. This method further enhances the design space of materials and is more conducive to optimization.

The main objective of this paper is to develop a computational framework that combines the MOACPSO algorithm and IGA for the size optimization of FGPs. The major characteristics of the present approach are summarized as follows: (a) any CVF distribution can be obtained, and it is not limited to a predefined function; (b) the sensitivity analysis is avoided compared with the conventional gradient methods, but it consumes more computation time; (c) the approach rapidly extends the coverage of the Pareto frontier; and (d) a series of optimal solutions are obtained, and the designer can select one optimal solution to meet the desired implementation. This combined method is presented here for the first time that is used to optimize the material distribution of FGPs. The MOCPSO has been improved and that forms a novel method, i.e., MOACPSO. In this study, we mainly focus our attention

on the multi-objective size optimization of FGPs using the optimization algorithm, and evaluating the MOACPSO in an all-round way according to some classical mathematical test functions and algorithm indexes is left for our further development.

The paper is organized as follows. Section 2 describes basic equations of free vibration for FGPs. The IGA model of natural frequency analysis of FGPs is presented in Section 3. Optimization problem is described in Section 4. Section 5 presents multi-objective adaptive chaotic particle swarm algorithm. Section 6 verifies the accuracy of B-spline functions for representing material distribution. In Section 7, the accuracy and performance of the proposed approach are demonstrated through four numerical examples. Finally, Section 8 describes some major conclusions arisen from the study.

## 2 Fundamental formulations

### 2.1 The FGPs

A ceramic-metal FGP with thickness  $h$  as schematically shown in Fig. 1 is considered. Material properties of FGP vary in the volume fractions through the plate thickness. We assume the bottom and top faces of plates to be fully metallic and ceramic, respectively.

In this study, Young's modulus  $E$  and the density  $\rho$  vary through the plate thickness. According to the simple rule of mixture (Vel and Batra 2002), Young's modulus and the density are given as

$$E(z) = E_c V_c(z) + E_m (1 - V_c(z)) \quad (1)$$

$$\rho(z) = \rho_c V_c(z) + \rho_m (1 - V_c(z)) \quad (2)$$

where  $V_c(z)$  represents the CVF, and subscripts  $c$  and  $m$  denote the ceramic and metal constituents, respectively.

There are some available models to describe the variation of the CVF, such as power function, exponential function, and three-parameter function.

- (1) Power function (Moita et al. 2018)

$$V_c^1 = \left( \frac{1}{2} + \frac{z}{h} \right)^n \quad (3)$$

where  $n$  is the material gradient index.

- (2) Exponential function (Woodward and Kashtalyan 2011)

$$V_c^2 = \frac{\vartheta_m e^{\left(\frac{1}{h} \ln \left(\frac{\vartheta_c}{\vartheta_m}\right) (z+h/2)\right)} - \vartheta_m}{\vartheta_c - \vartheta_m} \quad (4)$$

where  $\vartheta_c$  and  $\vartheta_m$  represent the properties of ceramic and metal materials, respectively. The material properties of each of the constituents consist of Young's modulus, Poisson's ratio, or density (Lieu et al. 2018).

(3) Three-parameter function (Zhu and Sankar 2007)

$$V_c^3 = \left( \frac{1}{2} + \frac{z}{h} + b \left( \frac{1}{2} - \frac{z}{h} \right)^n \right)^\gamma \quad (5)$$

where  $n$ ,  $b$ , and  $\gamma$  are the material gradient indexes.

The variation of the CVF can greatly alter the material properties, so the optimization of the CVF distribution of FGPs is investigated in this study.

## 2.2 The theory of S-FSDT

According to the S-FSDT (Yu et al. 2015; Liu et al. 2017a; Vu et al. 2017; Yin et al. 2014), the displacement fields can be expressed as

$$u(x, y, z) = u_0(x, y) - z w_{b,x} \quad (6a)$$

$$v(x, y, z) = v_0(x, y) - z w_{b,y} \quad (6b)$$

$$w(x, y, z) = w_b(x, y) + w_s(x, y) \quad (6c)$$

where  $u_0$  and  $v_0$  respectively represent the displacements at the mid-plane of the plate in the  $x$  and  $y$  directions;  $w_b$  and  $w_s$  respectively represent the bending component and the shear component of the transverse displacement at the mid-plane of the plate.

The expression of the strain-displacement relation is

$$\boldsymbol{\varepsilon} = \begin{Bmatrix} \boldsymbol{\varepsilon}_0 \\ 0 \end{Bmatrix} + \begin{Bmatrix} -z\boldsymbol{\kappa} \\ \boldsymbol{\gamma} \end{Bmatrix} \quad (7)$$

with

$$\boldsymbol{\varepsilon} = [\varepsilon_x \quad \varepsilon_y \quad \gamma_{xy} \quad \gamma_{yz} \quad \gamma_{xz}]^T \quad (8a)$$

$$\boldsymbol{\varepsilon}_0 = [u_{0,x} \quad v_{0,y} \quad u_{0,y} + v_{0,x}]^T \quad (8b)$$

$$\boldsymbol{\kappa} = [w_{b,xx} \quad w_{b,yy} \quad 2w_{b,xy}]^T \quad (8c)$$

$$\boldsymbol{\gamma} = [w_{s,x} \quad w_{s,y}]^T \quad (8d)$$

According to Hooke's law, the stress can be expressed as

$$\boldsymbol{\sigma} = \bar{\mathbf{D}}\boldsymbol{\varepsilon}, \boldsymbol{\tau} = \bar{\mathbf{G}}\boldsymbol{\gamma} \quad (9)$$

with

$$\boldsymbol{\sigma} = [\sigma_x \quad \sigma_y \quad \tau_{xy}]^T \quad (10a)$$

$$\bar{\mathbf{D}} = \frac{E(z)}{1+\nu} \begin{bmatrix} 1 & \nu & 0 \\ \frac{1-\nu}{\nu} & \frac{1-\nu}{\nu} & 0 \\ 0 & 0 & \frac{1}{2} \end{bmatrix} \quad (10b)$$

$$\boldsymbol{\tau} = [\tau_{xz} \quad \tau_{yz}]^T \quad (10c)$$

$$\bar{\mathbf{G}} = \frac{kE(z)}{2(1+\nu)} \begin{bmatrix} 1 & 0 \\ 0 & 1 \end{bmatrix} \quad (10d)$$

where  $\nu$  is the Poisson's ratio and the shear correction factor,  $k=5/6$ , is taken for the analysis. It is well reported in the literature that (also see the previous studies, see refs. (Yu et al. 2015; Liu et al. 2017a; Vu et al. 2017; Yin et al. 2014)) the shear correction factor,  $k=5/6$ , is reasonable for the analysis of FGM (functionally graded material) plates. However, this shear correction factor is no longer required when the high-order shear deformation theories are used.

## 2.3 Weak form of free vibration

The weak-form for natural frequency analysis of plate is derived using Hamilton's principle (Reddy 2004).

$$\int_0^T (\delta U - \delta K) dt = 0 \quad (11)$$

where  $\delta U$  and  $\delta K$  are the variation of strain energy and kinetic energy, respectively.

$$\delta U = \int_{\Omega} \left( \begin{Bmatrix} \delta \boldsymbol{\varepsilon}_0 & \delta \boldsymbol{\kappa} \end{Bmatrix} \begin{bmatrix} \mathbf{D}^m & \mathbf{B}^m \\ \mathbf{B}^m & \mathbf{D}^b \end{bmatrix} \begin{Bmatrix} \boldsymbol{\varepsilon}_0 \\ \boldsymbol{\kappa} \end{Bmatrix} + \delta \boldsymbol{\gamma}^T \mathbf{D}_s \boldsymbol{\gamma} \right) d\Omega \quad (12)$$

where  $\mathbf{D}^m = \int_{-h/2}^{h/2} \bar{\mathbf{D}} dz$ ,  $\mathbf{B}^m = \int_{-h/2}^{h/2} z \bar{\mathbf{D}} dz$ ,  $\mathbf{D}^b = \int_{-h/2}^{h/2} z^2 \bar{\mathbf{D}} dz$  and  $\mathbf{D}_s = \int_{-h/2}^{h/2} \bar{\mathbf{G}} dz$ .

$$\delta K = \int_{\Omega} \delta \mathbf{u}^T \mathbf{m} \ddot{\mathbf{u}} d\Omega \quad (13)$$

where  $\mathbf{u} = \{ \mathbf{u}_1 \quad \mathbf{u}_2 \}^T$ ,  $\mathbf{u}_1 = \{ u_0 \quad v_0 \quad w_b + w_s \}^T$ ,  $\mathbf{u}_2 = \{ w_{b,x} \quad w_{b,y} \quad 0 \}^T$ ,  $\mathbf{m} = \begin{bmatrix} I_0 & I_1 \\ I_1 & I_2 \end{bmatrix}$ , and the mass inertias are defined as

$$(I_0, I_1, I_2) = \int_{-h/2}^{h/2} \rho(z) (1, z, z^2) dz \quad (14)$$

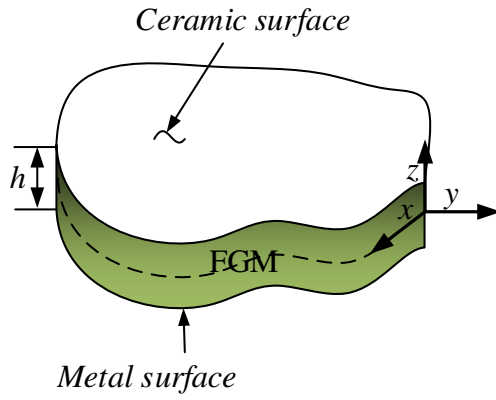


Fig. 1 Schematic of a classical ceramic-metal FGP

### 3 IGA model of free vibration analysis of FGPs

#### 3.1 A brief on the NURBS basis functions

For the sake of completeness, the basic knowledge of the NURBS basis functions is presented here. In the parametric space  $\xi \in [0, 1]$ , a knot vector is defined as a set of non-decreasing numbers, i.e.,  $\mathbf{k}(\xi) = \{\xi_1 = 0, \dots, \xi_i, \dots, \xi_{n+p+1} = 1\}^T$ , where  $i$  is the knot index and  $\xi_i$  is the  $i$ th knot, and  $\xi_i \leq \xi_{i+1}$ ;  $n$  is the number of basis functions. For the two-dimensional problem, the NURBS basis function is made up of a tensor product of one dimension B-spline basis function in two directions:

$$R_{i,j}^{p,q}(\xi, \eta) = \frac{N_{i,p}(\xi)N_{j,q}(\eta)w_{i,j}}{\sum_{i=1}^n \sum_{j=1}^m N_{i,p}(\xi)N_{j,q}(\eta)w_{i,j}} \quad (15)$$

where  $w_{i,j}$  is the weight,  $N_{i,p}(\xi)$  is the B-spline basis functions of order  $p$  in the  $\xi$  direction, and  $N_{j,q}(\eta)$  is the B-spline basis functions of order  $q$  in the  $\eta$  direction.

According to refs. (Hughes et al. 2005; Tornabene et al. 2016), the B-spline basis function  $N_{i,p}(\xi)$  is defined recursively for a given knot vector  $\mathbf{k}(\xi)$ :

$$N_{i,0}(\xi) = \begin{cases} 1 & \xi_i \leq \xi < \xi_{i+1} \\ 0 & \xi \geq \xi_{i+1} \text{ or } \xi < \xi_i \end{cases} \text{ for } p = 0 \quad (16a)$$

and

$$N_{i,p}(\xi) = \frac{\xi - \xi_i}{\xi_{i+p} - \xi_i} N_{i,p-1}(\xi) + \frac{\xi_{i+p+1} - \xi}{\xi_{i+p+1} - \xi_{i+1}} N_{i+1,p-1}(\xi) \quad \text{for } p \geq 1 \quad (16b)$$

$N_{j,q}(\eta)$  follows the same recursive formula in (16) with the knot vector  $\mathbf{k}(\eta)$ , and the definition of  $\mathbf{k}(\eta)$  is the same as that of  $\mathbf{k}(\xi)$ .

#### 3.2 Finite element model based on NURBS basis functions

Based on refs. (Yu et al. 2015; Liu et al. 2017a; Yin et al. 2014), the approximation of the generalized displacements in the mid-plane is expressed as

$$\mathbf{u}^h = \sum_{I=1}^{NC} R_I \mathbf{u}_I \quad (17)$$

with

$$\mathbf{u}_I = [u_0 \quad v_0 \quad w_b \quad w_s]^T \quad (18)$$

where  $NC = (p+1)(q+1)$  is the number of control points per element,  $R_I$  is the shape functions, and  $\mathbf{u}_I$  is the unknown displacement vector at control point  $I$ .

Substituting (17) into (8b)–(8d) yields

$$\{\varepsilon_0 \quad \kappa \quad \gamma\}^T = \sum_{I=1}^{NC} \{\mathbf{B}_I^m \quad \mathbf{B}_I^b \quad \mathbf{B}_I^s\}^T \mathbf{u}_I \quad (19)$$

with

$$\mathbf{B}_I^m = \begin{bmatrix} R_{I,x} & 0 & 0 & 0 \\ 0 & R_{I,y} & 0 & 0 \\ R_{I,y} & R_{I,x} & 0 & 0 \end{bmatrix} \quad (20a)$$

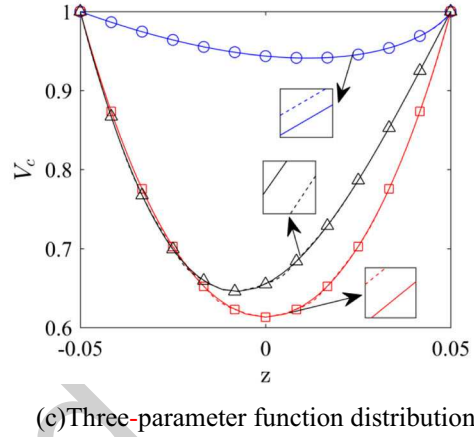
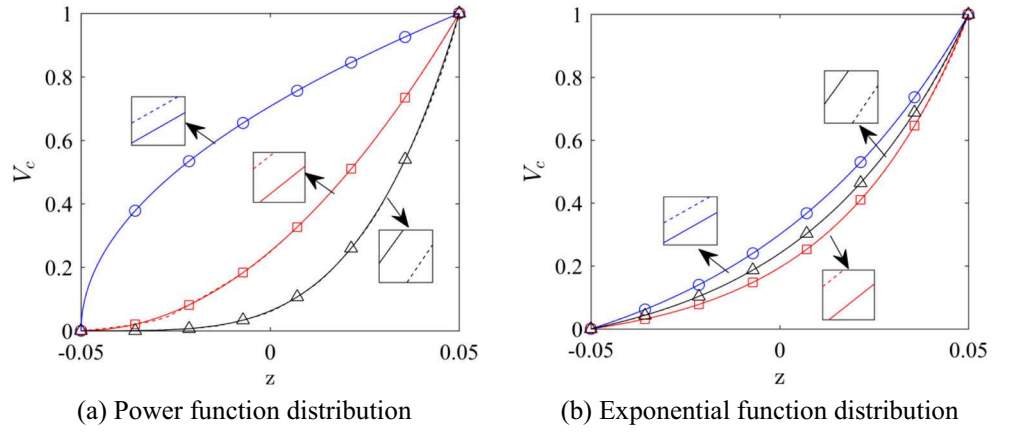
$$\mathbf{B}_I^b = \begin{bmatrix} 0 & 0 & R_{I,xx} & 0 \\ 0 & 0 & R_{I,yy} & 0 \\ 0 & 0 & 2R_{I,xy} & 0 \end{bmatrix} \quad (20b)$$

$$\mathbf{B}_I^s = \begin{bmatrix} 0 & 0 & 0 & R_{I,x} \\ 0 & 0 & 0 & R_{I,y} \end{bmatrix} \quad (20c)$$

Table 1 The values of parameters

Function type	Color			Number of control points
	Blue	Red	Black	
$V_c^1$	$n = 0.5$	$n = 2$	$n = 4$	8
$V_c^2$	$\vartheta_m = 7, \vartheta_c = 38$	$\vartheta_m = 3, \vartheta_c = 51$	$\vartheta_m = 1.44, \vartheta_c = 14.4$	8
$V_c^3$	$b = 1, n = 1.1, \gamma = 1.7$	$b = 1, n = 2, \gamma = 1.7$	$b = 1, n = 2, \gamma = 0.9$	13

**Fig. 2** Comparison of the CVF distribution between the general function description and the B-spline function description. **a** Power function distribution. **b** Exponential function distribution. **c** Three-parameter function distribution



Substituting (17) and (19) into (11), the discrete equation for free vibration problem holds

$$(\mathbf{K} - \omega^2 \mathbf{M}) \mathbf{u} = 0 \quad (21)$$

where  $\mathbf{K}$  and  $\mathbf{M}$  are the global stiffness matrix and the mass matrix, respectively.

The element contributions to  $K$  and  $M$  are:

$$\mathbf{k}^e = \int_{\Omega_e} \sum_{l=1}^{NC} \left[ \begin{Bmatrix} \mathbf{B}_l^m \\ \mathbf{B}_l^b \end{Bmatrix}^T \begin{bmatrix} \mathbf{D}^m & \mathbf{B}^m \\ \mathbf{B}^m & \mathbf{D}^b \end{bmatrix} \begin{Bmatrix} \mathbf{B}_l^m \\ \mathbf{B}_l^b \end{Bmatrix} + (\mathbf{B}_l^s)^T \mathbf{D}_s \mathbf{B}_l^s \right] d\Omega \quad (22a)$$

$$\mathbf{m}^e = \int_{\Omega_e} \sum_{l=1}^{NC} \mathbf{N}^T \mathbf{m} \mathbf{N} dx dy \quad (22b)$$

with

$$\mathbf{N} = [\mathbf{N}_1 \quad \mathbf{N}_2]^T \quad (23a)$$

$$\mathbf{N}_1 = \begin{bmatrix} R_l & 0 & 0 & 0 \\ 0 & R_l & 0 & 0 \\ 0 & 0 & R_l & R_l \end{bmatrix} \quad (23b)$$

**Table 2** Parameter settings in optimization algorithms

Parameter setting	Optimization algorithm		
	NSGA-II	MOPSO	MOACPSO
Common parameters	$N=100, T_{\max}=300, \bar{n}_{pf}=500, c_1=c_2=1.4955.$		
Personality parameters	Other parameters are referred by ref. (Deb et al. 2002)	Other parameters are referred by ref. (Bosman and Thierens 2003)	$w_s=0.9, w_f=0.4, \alpha_s=0.1, \sigma_s=0.3, u_0=0.5, y_0=0.5, T_c=200, \vartheta=0.1, \gamma_s=3, N_s=20.$

**Table 3** Parameters of material

	$E$ (GPa)	$\nu$	$\rho$ (kg/m <sup>3</sup> )
Metal (Al)	70	0.3	2707
Ceramic (Al <sub>2</sub> O <sub>3</sub> )	380	0.3	3800

$$\mathbf{N}_2 = \begin{bmatrix} 0 & 0 & R_{I,x} & 0 \\ 0 & 0 & R_{I,y} & 0 \\ 0 & 0 & 0 & 0 \end{bmatrix} \quad (23c)$$

#### 4 Optimization problem

According to ref. (Miettinen 1999), the general mathematical formulation of a multi-objective optimization problem is described as

$$\min_{\mathbf{x}_k} F(\mathbf{x}) = (f_1(\mathbf{x}), f_2(\mathbf{x}), \dots, f_n(\mathbf{x}))^T \quad (24)$$

subject to

$$h_i(\mathbf{x}) = 0 \quad i = 1, 2, \dots, n_h \quad (25a)$$

$$g_j(\mathbf{x}) \leq 0 \quad j = 1, 2, \dots, n_g \quad (25b)$$

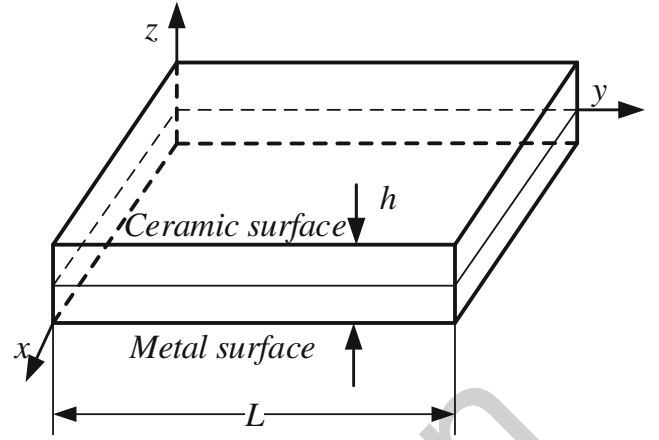
$$x_{k,\min} \leq x_k \leq x_{k,\max} \quad k = 1, 2, \dots, n_x \quad (25c)$$

where  $f_i$  is the  $i$ th objective, which depends on the design variables  $\mathbf{x}$ ; the functions  $h_i$  and  $g_j$  represent the equality constraints and inequality constraints, respectively;  $n_h$ ,  $n_g$ , and  $n_x$  are the number of equality constraints, inequality constraints, and design variables, respectively. In (25c),  $x_{k,\max}$  and  $x_{k,\min}$  are the upper and lower bounds of the design variable  $x_k$ , respectively.

In a multi-objective optimization problem, conflicts often occur among the objective functions; this means that there is no optimal solution for multi-objective optimization problem. In general, we only can obtain a non-inferior optimal solution of the multi-objective optimization model, which is called Pareto optimal solution. According to ref. (Bosman and Thierens 2003), the Pareto optimal solution is defined by:

**Table 4** First normalized natural frequency of Al/Al<sub>2</sub>O<sub>3</sub> square plates

Number of control points	$a/h = 10$			$a/h = 4$		
	$n = 0.5$	$n = 1$	$n = 5$	$n = 0.5$	$n = 1$	$n = 5$
$6 \times 6$	4.8982	4.4149	3.7831	26.713	24.102	20.242
$8 \times 8$	4.8960	4.4126	3.7811	26.702	24.092	20.233
$10 \times 10$	4.8957	4.4124	3.7809	26.701	24.091	20.232
$12 \times 12$	4.8957	4.4124	3.7809	26.701	24.091	20.232

**Fig. 3** A square FGP model

- (1)  $\mathbf{x}_v$  and  $\mathbf{x}_u$  are two feasible solutions, and they meet the relationships as follows:  
 $(\forall i = 1, 2, \dots, n: f_i(\mathbf{x}_v) \leq f_i(\mathbf{x}_u)) \wedge (\exists j = 1, 2, \dots, n: f_j(\mathbf{x}_v) < f_j(\mathbf{x}_u))$ , then  $\mathbf{x}_v$  is called to dominate  $\mathbf{x}_u$  (denoted  $\mathbf{x}_v < \mathbf{x}_u$ );
- (2)  $\mathbf{x}_v$  is called a Pareto optimal solution if  $\neg \exists \mathbf{x}_u: \mathbf{x}_u > \mathbf{x}_v$ .

In order to represent the CVF distribution, the CVFs at control points along the plate thickness are interpolated with the B-spline basis functions. The B-spline basis functions possess the feature of high-order continuity, so the material properties in the thickness direction can alter continuously and smoothly. In this study, the CVF distribution can be expressed as

$$V_c(\xi) = \sum_{i=1}^{np} N_{i,p}(\xi) V_c^i(z) \quad (26)$$

where  $np$  is the number of control points and  $V_c^i(z)$  is the CVF at the  $i$ th control point. According to the properties of B-spline basis function, it is obvious that the volume fraction interpolated with (26) always strictly satisfies the constraint  $0 \leq V_c \leq 1$  without any additional conditions.

In this analysis, two objectives are considered, i.e., minimize the mass of the FGP and maximize the first natural frequency. The optimization problem can be mathematically expressed as follows



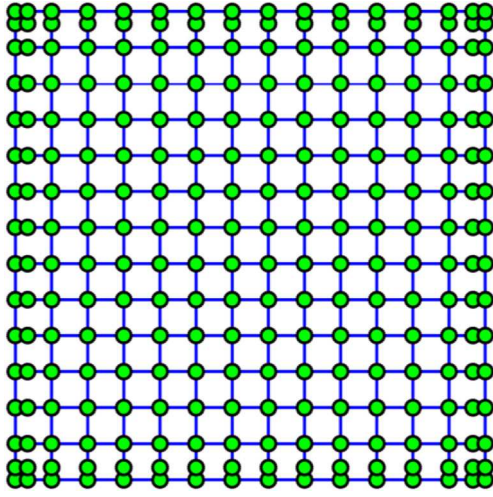


Fig. 4 Control points and physical mesh

$$\text{Minimize } f_1(\mathbf{V}_c) = \frac{1}{\omega_1} \quad \text{and} \quad f_2(\mathbf{V}_c) = \int_{\Omega} \int_{-h/2}^{h/2} \rho dz d\Omega \quad (27)$$

subject to

$$0 \leq V_c^i \leq 1, \quad i = 1, 2, \dots, np \quad (28)$$

where  $\mathbf{V}_c = [V_c^1, V_c^2, \dots, V_c^{np}]$  is the optimization variable vector and  $np$  is the number of variables,  $f_1$  and  $f_2$  are the corresponding objective functions, and  $\omega_1$  is the first natural frequency.

## 5 Multi-objective adaptive chaotic particle swarm algorithm

### 5.1 Particle swarm optimization algorithm

In 1995, Kennedy and Eberhart (1995) designed a new evolutionary optimization algorithm based on the bird predator behavior, i.e., particle swarm optimization (PSO) algorithm. The algorithm is simple and easy to implement. Furthermore, the speed of convergence by PSO is relatively fast, especially in the early stage of evolution. Compared with genetic algorithm (GA), there is no cross mutation process in the PSO scheme, but uses the random speed of individuals in space to change their position. Moreover, the information sharing mechanism is different among them. The information of GA is shared in a small scope, and chromosomes do a crossover operation one-to-one to exchange information. But PSO is global information sharing since the information sharing mechanism is a one-to-many relationship. On the one hand, each particle in PSO adjusts its search direction according to all previous flight experiences. On the other hand, all particles move towards the optimal value of the whole population, and all particles share the search experience of the whole population together.

Obviously, the PSO algorithm adjusts its evolutionary direction according to the optimal solution of the population history and the optimal solution of each particle itself. According to ref. (Kennedy and Eberhart 1995), the velocity and the position of the  $i$ th particle in the  $t$ th iteration are updated as

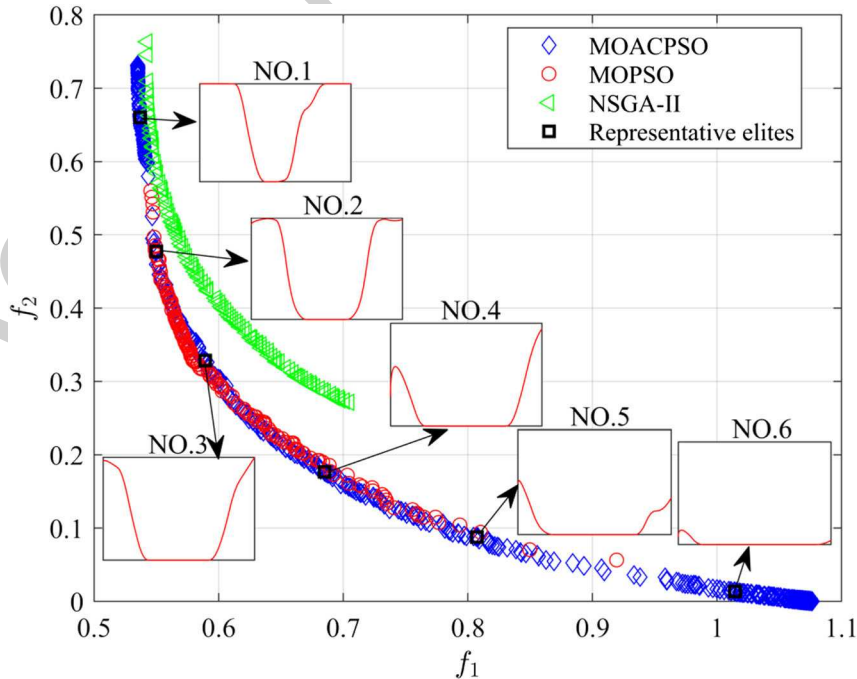
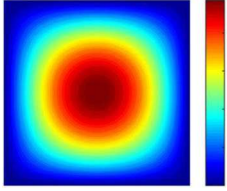

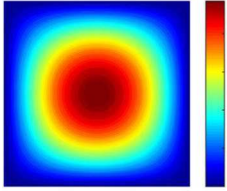
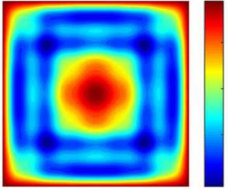
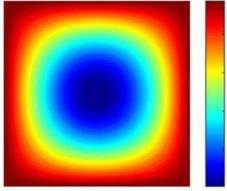

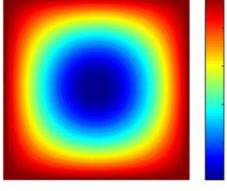
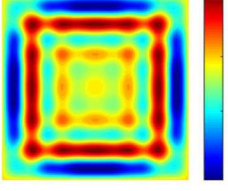
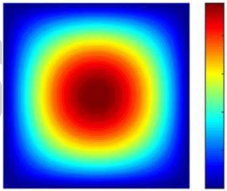
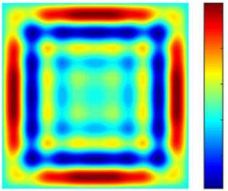
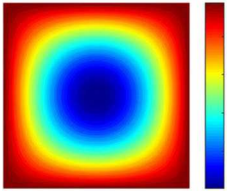
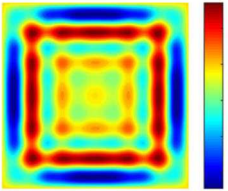


Fig. 5 The Pareto frontier of multi-objective design for the simply supported square FGP

**Table 5** The relevant statistical charts corresponding for the first mode shapes of the simply supported square FGP by representative elites

NO.	The first mode shapes	Numerical difference	NO. of the minuend
1			1
2			1
3			3
4			3
5			1
6			3

**Table 6** The result of representative elites

The objective function	No. of representative elite					
	1	2	3	4	5	6
$f_1$	0.5370 ( $3.478 \times 10^7$ )	0.5500 ( $3.306 \times 10^7$ )	0.5892 ( $2.880 \times 10^7$ )	0.6850 ( $2.131 \times 10^7$ )	0.8073 ( $1.535 \times 10^7$ )	1.0142 ( $9.722 \times 10^6$ )
$f_2$	0.6604 ( $3.429 \times 10^2$ )	0.4770 ( $3.228 \times 10^2$ )	0.3286 ( $3.066 \times 10^2$ )	0.1768 ( $2.900 \times 10^2$ )	0.0879 ( $2.803 \times 10^2$ )	0.0132 ( $2.721 \times 10^2$ )

\*The value in the bracket is the corresponding actual frequency (unit: Hz) or weight (unit: kg)

$$\mathbf{V}_i^{t+1} = \mathbf{V}_i^t + c_1 r_1 (\mathbf{P}_{i,best}^t - \mathbf{X}_i^t) + c_2 r_2 (\mathbf{G}_{best}^t - \mathbf{X}_i^t) \quad (29)$$

$$\mathbf{X}_i^{t+1} = \mathbf{X}_i^t + \mathbf{V}_i^{t+1} \quad (30)$$

where  $\mathbf{V}_i^t$  and  $\mathbf{X}_i^t$  are the velocity vector and position of the  $i$ th particle in the  $t$ th iteration, respectively;  $\mathbf{P}_{i,best}^t$  is the best position of the  $i$ th particle which is up to the  $t$ th iteration;  $\mathbf{G}_{best}^t$  is the best position of the whole particles up to the  $t$ th iteration;  $c_1$  and  $c_2$  are the learning factors; and  $r_1$  and  $r_2$  are random numbers from 0 to 1.

## 5.2 Multi-objective PSO algorithm

In 2004, Coello et al. (2004) proposed a multi-objective particle swarm optimization (MOPSO) algorithm by extending PSO to solve multi-objective optimization problems. The choice of  $\mathbf{G}_{best}^t$  and  $\mathbf{P}_{i,best}^t$  is a very important step in the MOPSO algorithm. Comparing the dominating relationship between  $\mathbf{P}_{i,best}^{t-1}$  and  $\mathbf{X}_i^t$ ,  $\mathbf{P}_{i,best}^t$  is updated with the corresponding dominating solution. If no dominance relation between  $\mathbf{P}_{i,best}^{t-1}$  and  $\mathbf{X}_i^t$  exists, one of them is randomly selected as  $\mathbf{P}_{i,best}^t$ . In the MOPSO, a particle is selected as  $\mathbf{G}_{best}^t$  based on the density information of particles in the external archive set.

In the MOPSO, the objective space is uniformly divided into some grids, and the number of particles contained in a grid is defined as the density information of the particle. The estimation method of the density information is as follows

(Coello et al. 2004): (1) compute the size of grid  $\Delta f_i^t$  with  $\Delta f_i^t = \frac{\max(f_i^t) - \min(f_i^t)}{M}$  for  $i = 1, 2, \dots, n$ , where  $f_i^t$  is the  $i$ th objective function in the  $t$ th iteration,  $M$  is the number of grids, and  $n$  is the number of objective functions; (2) compute the numbering of grid containing particle  $j$  with

**Table 7** Comparison of the solutions with different algorithms

Method	Crowding variance (CV)	Frontier spread (FS)	Set coverage (SC)
NSGA-II	0.0043	0.5453	0 / 0
MOPSO	0.0077	0.7254	0.9000 / 0.1106
MOACPSO	0.0040	1.0913	1 / 0.4600

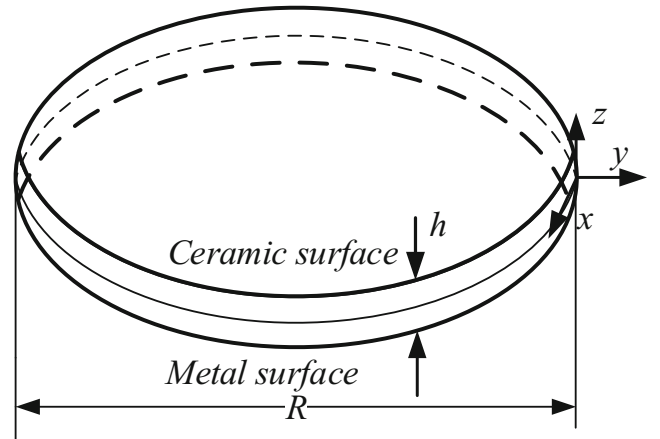
$\left( \text{Int} \left( \frac{f_i^t - \min(f_i^t)}{\Delta f_i^t} \right), \dots, \text{Int} \left( \frac{f_n^t - \min(f_n^t)}{\Delta f_n^t} \right) \right)$ ; and (3) compute the grid information and the density value of each particle.

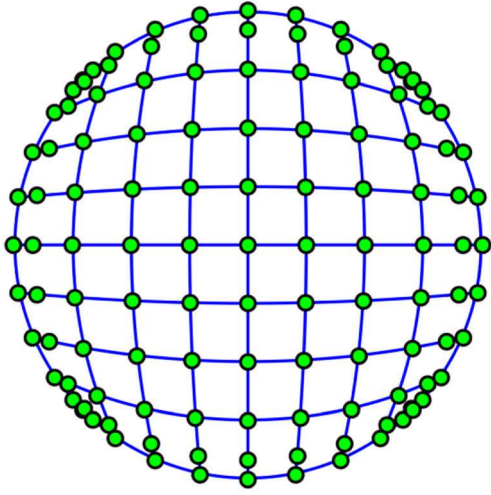
## 5.3 Multi-objective adaptive chaotic PSO algorithm

### 5.3.1 Chaos strategy updating of velocity

For multiple hump optimization problems, the bionic algorithm (e.g., particle swarm optimization algorithm, genetic algorithm, ant colony algorithm), which is a large class of heuristic algorithms, is easy to fall into local optimum (Alatas et al. 2009). In those algorithms, the quality of initial population directly determines the quality of optimization results. Although MOPSO algorithm has done some simple random disturbances at velocity updating, the effect of optimization is still imperfect. Therefore, it is necessary to design a strategy to jump out of local solutions.

The chaotic system is a random irregular motion produced by the non-linear deterministic system. The chaotic sequence generated by the chaotic function has the characteristics of uncertainty, unrepeatability, and unpredictability. Therefore, embedding the chaotic system into the optimization algorithm can make the candidate solution set more diversified, and thus avoid the local optimal solution (Alatas et al. 2009). There are many types of chaotic functions (Singh and Sinha 2010) such as Hénon map and Ikeda map. In this study, the chaotic sequence generated by Zaslavskii map (Zaslavskii 1978) is

**Fig. 6** Schematic of a circular FGP model



**Fig. 7** A circular FGP with  $11 \times 11$  control points and  $8 \times 8$  cubic elements

defined as follows:

$$y_{k+1} = \cos(2\pi u_k) + y_k e^{-3} \quad (31)$$

$$u_{k+1} = (u_k + 400 + 12y_{k+1}) \bmod(1) \quad (32)$$

where  $k$  is chaotic index and  $u_0$  and  $y_0$  are randomly generated from  $(0, 1)$ .

In this study, chaos randomization is applied to update candidate velocity, and (29) is rewritten as

$$\mathbf{V}_i^{t+1} = w\mathbf{V}_i^t + c_1 S_1^t (\mathbf{P}_{1,best}^t - \mathbf{X}_i^t) + c_2 S_2^t (\mathbf{G}_{best}^t - \mathbf{X}_i^t) \quad (33)$$

where  $S_1^t$  and  $S_2^t$  are randomly selected from the sequence  $\{u_k\}$ , the size of  $\{u_k\}$  is two times of the maximum iteration number  $T_{max}$ , and  $w$  is the inertia weight, which is defined as (Eberhart and Shi 2002):

$$w = w_s - \frac{(w_s - w_f)t}{T_{max}} \quad (34)$$

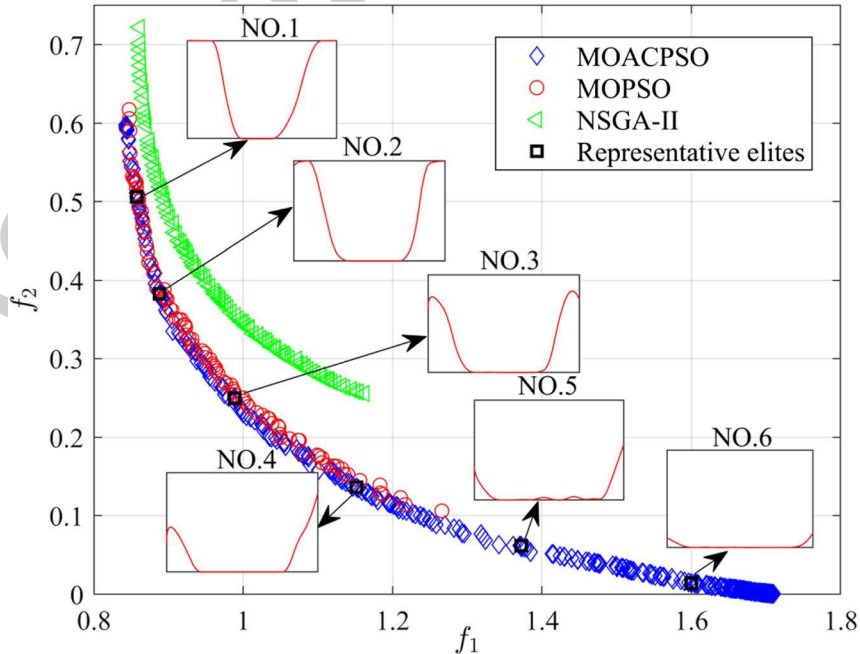
where  $w_s$  and  $w_f$  are the inertial weights of the first and the last times, respectively;  $t$  is the current iteration or generation number.

### 5.3.2 Adaptive strategy for fitness selection

From the structure of algorithm, the MOPSO algorithm has an additional construction and maintenance of the external archive compared with the PSO algorithm, so how to effectively make use of the limited space of the external archive is one of the key problems for the MOPSO algorithm. To avoid the crowding and distortion of the external archive, the sharing niche technique is used in the MOACPSO algorithm (Srinivas and Deb 1994), instead of the adaptive grid method in the MOPSO algorithm. The fitness function is defined as

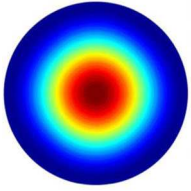
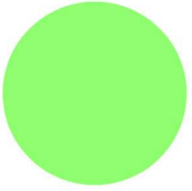
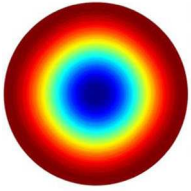

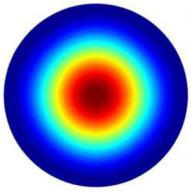
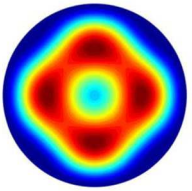
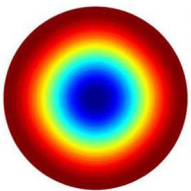
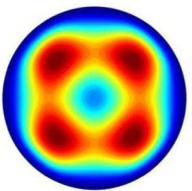
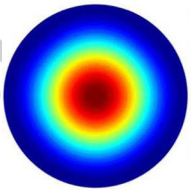
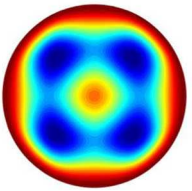
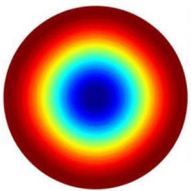
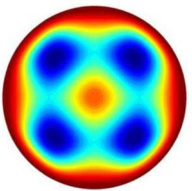
$$Fit(i) = \frac{1}{\sum_{j=1}^{n_{pf}} s(dis(i, j))} \quad (35)$$

where  $n_{pf}$  is the size of the current external archive,  $\mathbf{X}_i$  and  $\mathbf{X}_j$  belong to the external archive, and  $s(dis(i, j))$  is the sharing function between the particles  $i$  and the particles  $j$  in the external archive, which is defined as



**Fig. 8** The Pareto frontier of multi-objective design for the clamped circular FGP

**Table 8** The relevant statistical charts corresponding for the first mode shapes of the clamped circular FGP by representative elites

NO.	The first mode shapes	Numerical difference	NO. of the minuend
1			1
2			2
3			1
4			2
5			1
6			2

**Table 9** The result of representative elites

The objective function	No. of representative elite					
	1	2	3	4	5	6
$f_1$	0.8573 ( $1.361 \times 10^5$ )	0.8879 ( $1.268 \times 10^5$ )	0.9886 ( $1.023 \times 10^5$ )	1.1516 ( $7.541 \times 10^4$ )	1.3721 ( $5.312 \times 10^4$ )	1.6000 ( $3.906 \times 10^4$ )
$f_2$	0.5060 ( $1.024 \times 10^2$ )	0.3827 ( $9.818 \times 10^1$ )	0.2493 ( $9.360 \times 10^1$ )	0.1363 ( $8.972 \times 10^1$ )	0.0616 ( $8.716 \times 10^1$ )	0.0143 ( $8.553 \times 10^1$ )

\*The value in the bracket is the corresponding actual frequency (unit: Hz) or weight (unit: kg)

$$s(dis(i, j)) = \begin{cases} 1 - \left( \frac{dis(i, j)}{\sigma_s} \right)^{\alpha_s} & dis(i, j) < \sigma_s \\ 0 & dis(i, j) \geq \sigma_s \end{cases} \quad (36)$$

where  $\sigma_s$  is the allowed maximum phenotypic distance between two particles becoming members of a niche in the external archive,  $\alpha_s$  is the modified parameter of the sharing function,  $dis(i, j) = \|F(\mathbf{x}_i) - F(\mathbf{x}_j)\|$ ,  $F(\mathbf{x}_i)$ , and  $F(\mathbf{x}_j)$  are the multi-objective functions of  $\mathbf{X}_i$  and  $\mathbf{X}_j$ , respectively, and  $\mathbf{X}_i$  and  $\mathbf{X}_j$  belong to the external archive.

In order to accelerate the optimization process, the adaptive strategy for fitness selection is introduced, and the adaptation of (35) is described as

$$Fit_C(i) = \left( \frac{Fit(i) - \min\{Fit(j)\}}{\max\{Fit(j)\} - \min\{Fit(j)\}} \right)^{\gamma_s} \quad \text{for } j = 1, 2, \dots, n_{pf} \quad (37)$$

where  $\gamma_s$  is the adaptive parameter, which is generally greater than 0, and the larger the value of  $\gamma_s$  is, the greater the probability of the selected particle with maximum fitness is.

### 5.3.3 Directional perturbation mechanism of elite solutions

In order to expand the coverage of the Pareto frontier, the directional perturbation mechanism is made to the elite solutions located at both ends of the Pareto frontier. In the external archive of FGP optimization, the multi-objective functions of the  $i$ th elite solution  $X_s^i = \{x_s^i, x_s^i, \dots, x_s^i\}$  are  $\mathbf{FS}_i = \{f_s^i, f_s^i\}$  subjected to  $f_s^i \leq f_s^{i+1} \wedge f_s^i \geq f_s^{i+1}$ ,  $i \leq n_{pf}$ . The miniature particles are randomly generated from  $(\mathbf{X}_s^1 - \vartheta, \mathbf{X}_s^1 + \vartheta)$  and  $(\mathbf{X}_s^{n_{pf}} - \vartheta, \mathbf{X}_s^{n_{pf}} + \vartheta)$  at  $N_s$  times, and  $\vartheta$  is the perturbation radius whose value is small. Finally, the non-inferior solutions are selected from those particles and added to the external archive. Obviously, the directional perturbation mechanism by MOCAPSO is equivalent to the directional

**Table 10** Comparison of the solutions with different algorithms

Method	Crowding variance (CV)	Frontier spread (FS)	Set coverage (SC)
NSGA-II	0.0033	0.6154	0 / 0
MOPSO	0.0071	0.7757	1 / 0.0127
MOACPSO	0.0041	1.2351	1 / 0.8132

“mutation,” which is more targeted than the mutation in MOPSO. That is to say, each particle is mutated and the fitness is calculated again in MOPSO and number of function evaluations is  $2N \cdot T_{max}$ . But the directional perturbation of  $N_s$  times is carried out in each iteration in MOACPSO, so the number of function evaluations is  $N \cdot T_{max} + N_s$ .

In the MOACPSO algorithm,  $\mathbf{G}_{best}$  is selected from the external archive by the roulette wheel selection method using (37), and  $\mathbf{P}_{i, best}$  is updated to be the nearest elite solution from the external archive. Then, the particle position is updated according to (30) and (33), and non-inferiority solutions from the population are added to the external archive. If the size of the external archive exceeds the specified capacity, some elite solutions with worse fitness are eliminated until the reasonable capacity of the external archive is obtained.

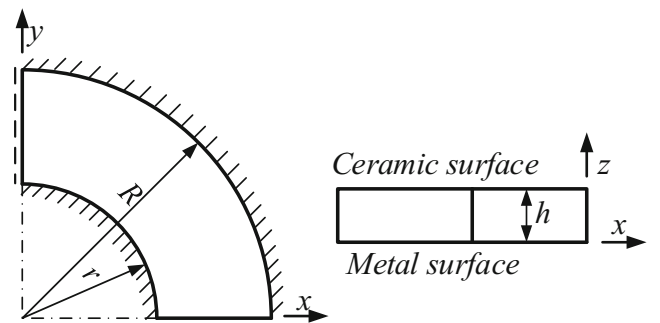
### 5.3.4 Numerical implementation

The main solution procedure of the MOACPSO is summarized as follows:

- (1) Randomly initialize particle swarm and generate the chaotic sequences  $\{u_k\}$ .
- (2) Loop over the number of iterations.
  - a. Update the inertia weight value with (34).
  - b. Loop over the number of particles.

Update the chaotic  $S_1$  and  $S_2$  value from  $\{u_k\}$ .

Update the position of particles with (33) and (30).

**Fig. 9** A quarter model of a circular FGP

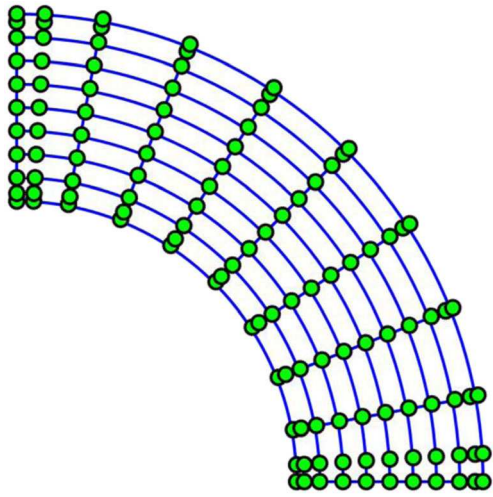


Fig. 10 Control points and physical mesh

Calculate the fitness of each individual by (37).

- c. Repeat the loop until the maximum number of particles.
  - d. Find non-inferior solutions and put them into the external archive.
  - e. Do the directional perturbation about the elite solutions at the two ends of the Pareto frontier.
  - f. Update the external archive.
  - g. Find  $P_{i, best}$  and  $G_{best}$ .
- (3) Repeat the loop until the maximum iteration step is reached.

## 6 Accuracy analysis of B-spline functions for representing material distribution

In this study, the material distribution is represented with the B-spline functions. To verify the accuracy of this method, CVF distribution described with function is compared with that represented with B-spline functions. Three functions including the power function (Moita et al. 2018), the exponential function (Woodward and Kashtalyan 2011), and the three-parameter function (Roque et al. 2016) are adopted to describe the CVF distribution. The thickness of the FGP is 0.1 units, and the quadratic B-spline basis functions are used. The values of parameters in distribution function are shown in Table 1. Figure 2 presents the comparison of the CVF distribution between the general function description and the B-spline function description. In the figures, the spots are the control points. The solid lines are drawn with the given functions, while the dash lines are B-spline curves. The solid line almost coincides with the dash line, and the partial enlarged details are presented to show the difference. The good agreement of CVF distribution from the given function distribution and the B-spline function can be found. It is noted that the material properties along the thickness direction vary continuously and smoothly using the quadratic B-spline functions.

## 7 Numerical examples and discussion

In this section, four numerical examples are considered to validate the accuracy and performance of the present method. Some simulations are described in the first

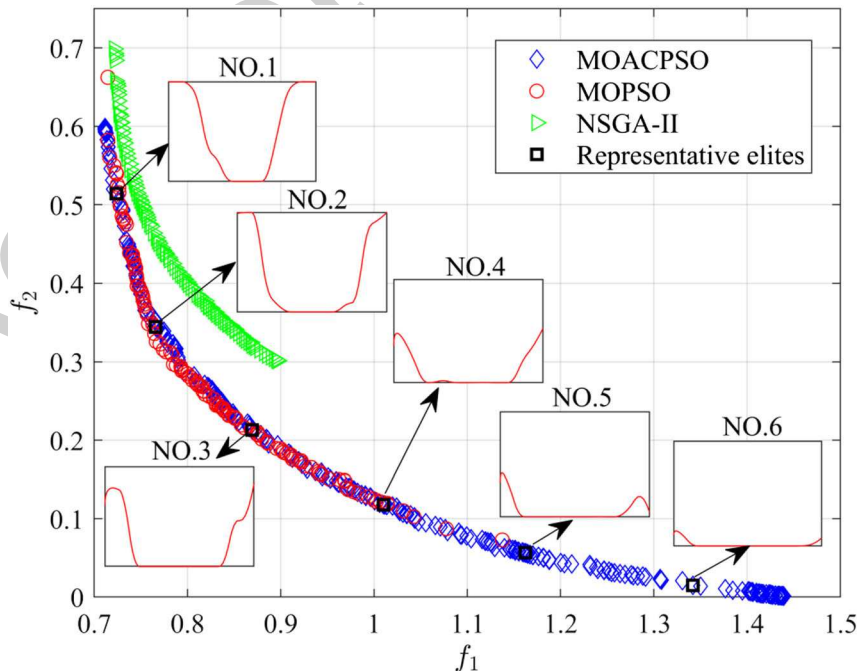
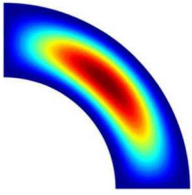

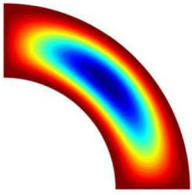

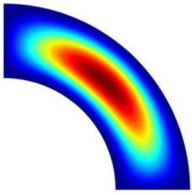
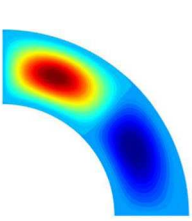
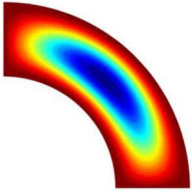
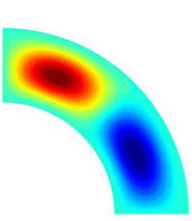
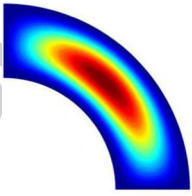
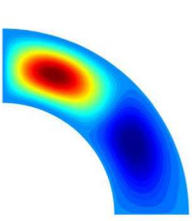
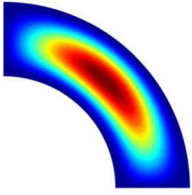
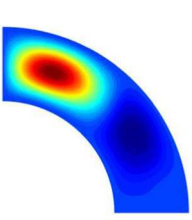


Fig. 11 The Pareto frontier of multi-objective design for the quarter of a circular FGP

**Table 11** The relevant statistical charts corresponding for the first mode shapes of the quarter of circular FGP by representative elites

NO.	The first mode shapes	Numerical difference	NO. of the minuend
1			1
2			2
3			1
4			2
5			1
6			1



example, and other numerical examples are consistent with the relevant definition in the first example if no special explanation is given. The NSGA-II, MOPSO, and MOACPSO algorithms are used. The parameter setting of the three algorithms is summarized in Table 2, where  $N$  represents the size of the population,  $T_{\max}$  is the maximum iteration number,  $\bar{n}_{pf}$  is the maximum size of the external archive, and  $T_c$  is the size of  $\{u_k\}$ . Moreover, the quadratic B-spline functions are used to describe the CVF distribution and the cubic NURBS basis functions are used in the IGA. Table 3 presents relevant material parameters.

Two objectives are considered, i.e., minimize the mass and maximize the first natural frequency. The design variables are the CVFs at control points in the thickness direction, and their values are between 0 and 1.

In general, the real Pareto frontier is unknown in the multi-objective optimization problems; so the traditional indicators cannot be used in optimization of FGPs. Fortunately, there exist some indicators to measure the performance of a multi-objective optimization algorithm. Three indicators are adopted in this study, and they are defined as follows:

- (1) Crowding variance (CV) (Schott 1995). CV shows the measure of uniformity about the distribution of all elite solutions on the Pareto frontier, and the smaller the value of CV is, the better the performance of the algorithm is. The CV is defined as

$$CV = \sqrt{\frac{\sum_{i=1}^l (\bar{d} - d_i)^2}{l-1}} \quad (38)$$

where  $d_i$  represents the distance between the  $i$ th elite solution and the  $j$ th elite solution in external archiving,  $\bar{d}$  is the mean of all  $d_i$ , and  $l = n_{pf} - 1$ . For two objectives,  $d_i$  can be expressed as

$$d_i = \sqrt{|f_1(\mathbf{X}^i) - f_1(\mathbf{X}^j)|^2 + |f_2(\mathbf{X}^i) - f_2(\mathbf{X}^j)|^2} \quad \text{for } j = i + 1 \quad (39)$$

- (2) Frontier spread (FS). FS is the coverage of the optimal solution set at the Pareto frontier, and the larger the value of FS is, the wider the coverage is. FS can be given as

**Table 12** The result of representative elites

The objective function	No. of representative elite					
	1	2	3	4	5	6
$\bar{J}_1$	0.7237 (1.910 × 10 <sup>7</sup> )	0.7660 (1.704 × 10 <sup>7</sup> )	0.8693 (1.323 × 10 <sup>7</sup> )	1.0101 (9.802 × 10 <sup>6</sup> )	1.1623 (7.402 × 10 <sup>6</sup> )	1.3417 (5.555 × 10 <sup>6</sup> )
$\bar{J}_2$	0.5143 (1.643 × 10 <sup>1</sup> )	0.3446 (1.550 × 10 <sup>1</sup> )	0.2130 (1.478 × 10 <sup>1</sup> )	0.1180 (1.426 × 10 <sup>1</sup> )	0.0565 (1.392 × 10 <sup>1</sup> )	0.0150 (1.369 × 10 <sup>1</sup> )

\*The value in the bracket is the corresponding actual frequency (unit: Hz) or weight (unit: kg)

**Table 13** Comparison of the solutions with different algorithms

Method	Crowding variance (CV)	Frontier spread (FS)	Set coverage (SC)
NSGA-II	0.0029	0.4573	0 / 0
MOPSO	0.0097	0.8385	1 / 0.2190
MOACPSO	0.0038	1.1090	1 / 0.2598

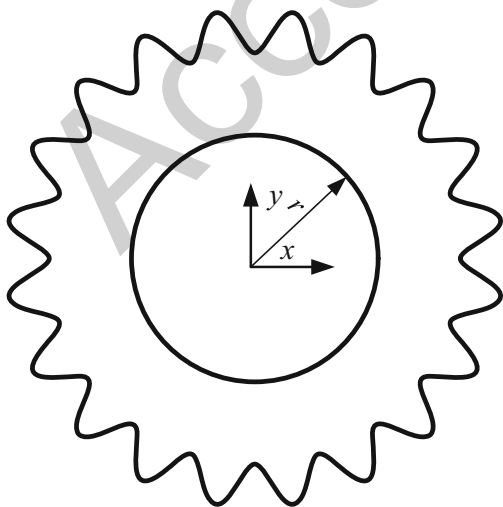
$$D_{nf} = \sum_i^{\bar{n}_{pf}} d_i \quad (40)$$

(3) Set coverage (SC) (Zitzler and Thiele 1999). SC provides an intuitive comparison of the performance of two algorithms, as follows:

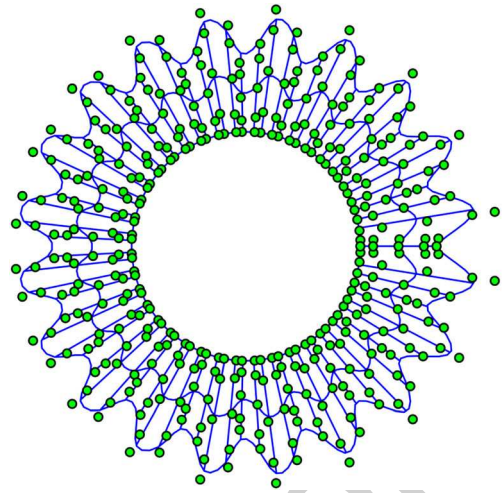
$$SC(K_s, K_o) = |\{k_o \in K_o | \exists k_s \in K_s : k_s < k_o\}| / |K_o| \quad (41)$$

where  $K_s$  and  $K_o$  are the external archiving of the two algorithms, respectively. The general situation of  $0 < SC(K_s, K_o) < 1$  is said that  $K_o$  is partially covered by  $K_s$ ,  $SC(K_s, K_o) = 1$  represents all solutions in  $K_o$  are strictly dominated by  $K_s$ , while  $SC(K_s, K_o) = 0$  means none of the solutions in  $K_o$  are covered by  $K_s$ . In the same way,  $SC(K_o, K_s)$  is similar to that of (41). Generally speaking, it can be explained that  $K_s$  is better than  $K_o$  in the case of  $SC(K_s, K_o) = 1$ .

The convergence study of the S-FDST-based IGA is first investigated before testing numerical optimization examples. A fully simply supported Al/Al<sub>2</sub>O<sub>3</sub> square plate with length-thickness ratio of  $a/h$  is considered. The volume fraction of the material satisfies the power function shown in (3). The first normalized natural frequency  $\bar{\omega} = 100\omega h \sqrt{\rho_c/E_c}$  obtained with different numbers of control points is listed in Table 4. It can be seen that it is fast to obtain the convergent results, so the S-FDST-based IGA has high accuracy and fast



**Fig. 12** A gear FGP with one circular hole



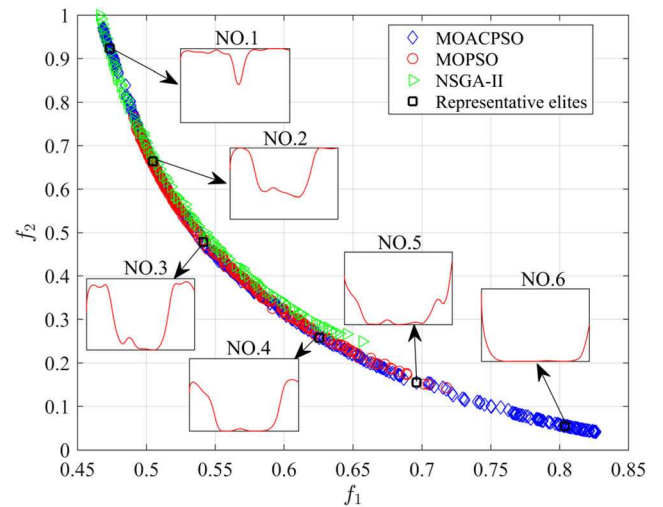
**Fig. 13** Control mesh with  $80 \times 5$  control points and  $77 \times 2$  cubic elements

convergence speed, and the convergent results are obtained with the control points of  $10 \times 10$ .

### 7.1 A simply supported square FGP

The first example deals with a simply supported square FGP shown in Fig. 3. The width of the plate is  $L = 1$  m and the thickness is  $h = 0.1$  m. The control mesh with  $13 \times 13$  cubic elements is shown in Fig. 4. The number of design variables is 16 for the CVFs at control points in the thickness direction. For the convenience of optimization, the mass and the first natural frequency of the FGP are normalized with  $\bar{V}_c(\mathbf{V}_c)$

$$= \frac{\int_{-h/2}^{h/2} V_c dz}{h} \quad \text{and} \quad \bar{\omega}(\mathbf{V}_c) = \frac{\omega L^2}{h\sqrt{1/10^9}}, \quad \text{respectively.}$$



**Fig. 14** The Pareto frontier of MOP design for the gear FGP with one hole

**Table 14** Relevant statistical charts corresponding for the first mode shapes of the gear FGP by representative elites

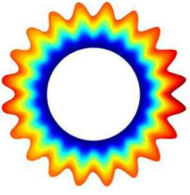

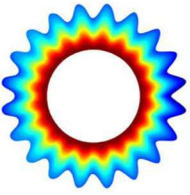
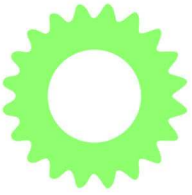
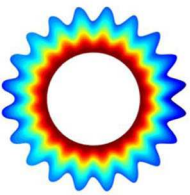
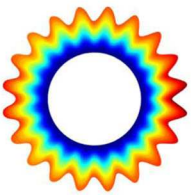
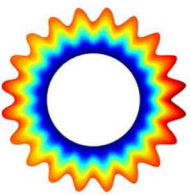
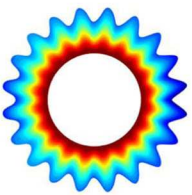
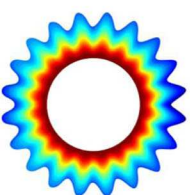
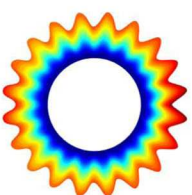
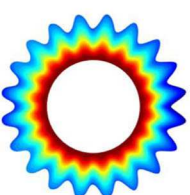
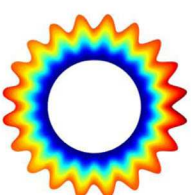
NO.	The first mode shapes	Numerical difference	NO. of the minuend
1	 <p>Heatmap of gear first mode shape 1. Color scale ranges from 0 (blue) to 0.4 (red).</p>	 <p>Heatmap of gear numerical difference 1. Color scale ranges from -1 (blue) to 1 (red).</p>	1
2	 <p>Heatmap of gear first mode shape 2. Color scale ranges from -0.4 (blue) to -0.1 (red).</p>	 <p>Heatmap of gear numerical difference 2. Color scale ranges from -1 (blue) to 1 (red).</p>	2
3	 <p>Heatmap of gear first mode shape 3. Color scale ranges from -0.3 (blue) to -0.1 (red).</p>	 <p>Heatmap of gear numerical difference 3. Color scale ranges from 0 (blue) to 0.04 (red).</p>	2
4	 <p>Heatmap of gear first mode shape 4. Color scale ranges from 0 (blue) to 0.3 (red).</p>	 <p>Heatmap of gear numerical difference 4. Color scale ranges from -0.15 (blue) to -0.05 (red).</p>	1
5	 <p>Heatmap of gear first mode shape 5. Color scale ranges from -0.3 (blue) to -0.1 (red).</p>	 <p>Heatmap of gear numerical difference 5. Color scale ranges from 0 (blue) to 0.04 (red).</p>	2
6	 <p>Heatmap of gear first mode shape 6. Color scale ranges from -0.3 (blue) to -0.1 (red).</p>	 <p>Heatmap of gear numerical difference 6. Color scale ranges from 0 (blue) to 0.01 (red).</p>	2

Figure 5 shows the Pareto frontier of the multi-objective optimization problem for the simply supported square FGP. In addition, the sub-figures in Fig. 5 represent the ceramic distribution corresponding to the partial elite solution. The first mode shapes of representative elites are shown in Table 5; it can be seen that their values are almost the same or opposite. The difference between the first mode shapes is used to distinguish them and the corresponding number of the minuend can be referred to Table 5. Table 6 reports the result of representative elites. Table 7 gives the performance statistics of the three algorithms, and it can be seen that all aspects of MOACPSO are superior to those of MOPSO and NSGA-II.

## 7.2 A clamped circular FGP

As shown in Fig. 6, a clamped circular FGP with a radius of  $R$  and a thickness of  $h$  is considered.  $h = 0.01$  m,  $R = 1$  m. The normalized frequency is  $\bar{\omega}(\mathbf{V}_c) = \omega R^2 / h \sqrt{1/10^9}$ . The circular FGP is divided into  $11 \times 11$  control points and  $8 \times 8$  cubic elements for IGA as sketched in Fig. 7, and the number of design variables is 16 for the CVFs at control points in the thickness direction.

Similar to the first numerical example, the Pareto frontier of the multi-objective optimization problem for the clamped circular FGP is shown in Fig. 8, while Table 8 depicts the first mode shapes of representative elites. The result of representative elites is given in Table 9. Table 10 gives the performance statistics of the three algorithms, and it can be seen that the value of CV for NSGA-II is smaller, but its solutions is completely dominated by MOACPSO, which means that the solution of NSGA-II is meaningless. Moreover, all aspects of MOACPSO are better than those of MOPSO.

## 7.3 A quarter of circular FGP with complex boundaries

Consider a quarter of circular FGP with clamped inner and outer boundaries and simply supported at left and bottom sides, as shown in Fig. 9. The outer radius is  $R = 1$  m and inner radius is  $r = 0.6$  m and the thickness is  $h = 0.01$  m. Figure 10 presents the control points and physical mesh for IGA, and the number of design variables is 16 for the CVFs at control points in the thickness. The normalized frequency is  $\bar{\omega}(\mathbf{V}_c) = \omega R^2 / h \sqrt{1/10^{11}}$ .

The Pareto frontier of the multi-objective optimization problem for the quarter of a circular FGP is shown in Fig. 11, while Table 11 presents the first mode shapes of representative elites. And the result of representative elites is given in Table 12. The performance statistics of the two algorithms is shown in Table 13, and it is obvious that MOACPSO is superior to MOPSO and covered the solution set of NSGA-II.

**Table 15** The result of representative elites

The objective function	No. of representative elite					
	1	2	3	4	5	6
$f_1$	0.4734 (4.462 × 10 <sup>7</sup> )	0.5048 (3.924 × 10 <sup>7</sup> )	0.5414 (3.412 × 10 <sup>7</sup> )	0.6256 (2.555 × 10 <sup>7</sup> )	0.6961 (2.064 × 10 <sup>7</sup> )	0.8040 (1.547 × 10 <sup>7</sup> )
$f_2$	0.9238 (1.012 × 10 <sup>3</sup> )	0.6638 (9.344 × 10 <sup>2</sup> )	0.4787 (8.794 × 10 <sup>2</sup> )	0.2579 (8.137 × 10 <sup>2</sup> )	0.1551 (7.831 × 10 <sup>2</sup> )	0.0545 (7.532 × 10 <sup>2</sup> )

\*The value in the bracket is the corresponding actual frequency (unit: Hz) or weight (unit: kg)

**Table 16** Comparison of the solutions with different algorithms

Method	Crowding variance (CV)	Frontier spread (FS)	Set coverage (SC)
NSGA-II	0.0043	0.7931	0 / 0.1068
MOPSO	0.0031	0.7192	0.74 / 0.2397
MOACPSO	0.0027	1.0878	0.73 / 0.4699

## 7.4 A gear FGP with one circular hole

The last numerical example deals with an FGP with one circular hole and 20 gear teeth as shown in Fig. 12. The main purpose of considering this gear teeth example having complicated geometries is to demonstrate the applicability of the developed approach. In particular, the geometry parameters of the example are set as follows. The radius of the hole is  $r = 0.6$  m, and the thickness  $h$  is 0.1 m. The outer boundary  $\Gamma$  can be expressed by a mathematical formula as

$$\Gamma = \{ R\cos(\theta) \quad R\sin(\theta) \} \quad (42)$$

with

$$R = (n^2 + 2n + 2 - 2(n + 1)\cos(n\theta))/n^2 \quad (43)$$

where  $n$  is the number of gear teeth, and the range of  $\theta$  is 0 to  $2\pi$ .

The hole boundary is clamped when the gear is fixed to the shaft in mechanical engineering. As shown in Fig. 13, the computation domain is divided into  $80 \times 5$  control points and  $77 \times 2$  cubic elements for IGA. The number of design variables is 16 for the CVFs at control points in the thickness. The normalized frequency is  $\bar{\omega}(\mathbf{V}_c) = \omega/h\sqrt{1/10^9}$ .

Figure 14 illustrates the Pareto frontier of MOP design for the gear FGP with one hole, and the first mode shapes of the representative elites are visualized in Table 14. The obtained result of representative elites is given in Table 15, while Table 16 reports the performance statistics of the three algorithms. And the simulation results prove that MOACPSO is better than MOPSO and NSGA-II in all aspects as the previous results.

## 8 Conclusions

We have developed an effective multi-objective optimization methodology that combines the IGA with S-FSDT and adaptive chaos particle swarm algorithm for optimizing CVF distribution of FGPs under free vibration. The CVF distribution is described with the B-spline basis functions via control points along the thickness direction. The plate free vibration analysis is conducted by using NURBS-based IGA and an effective plate theory, the S-FSDT. Minimizing the mass of

the structure and maximizing the first natural frequency are two optimization objectives. The adaptive chaotic particle swarm algorithm is used as an optimizer. From the results of four representative numerical examples, several major conclusions are drawn as follows:

- The B-spline-based volume fraction representation has few design variables, and the material properties in FGPs with any complex distribution profile can alter continuously and smoothly.
- Compared with MOPSO and NSGA-II, the performance of the adaptive chaotic particle swarm algorithm has been improved in CV, FS, and SC.
- The optimal CVF distributions can be entirely different from those described by the certain mathematical function, broadening the material variability.
- It is possible to select one optimal solution by designers to meet the desired implementation according to a series of optimal solutions.
- From physical interpretation of the optimization results, when choosing the best solution with higher quality, the proportion of ceramics on the top and bottom of FGPs will be higher while the proportion of ceramics on the middle of FGPs will be lower. In addition, the smaller the ceramic fraction, the smaller the corresponding mass and frequency.

**Acknowledgments** The authors would like to thank all the anonymous referees for their valuable comments and suggestions to further improve the quality of this work.

**Funding information** This work was supported by the National Natural Science Foundation of China (Grant No. 61375068) and the Fundamental Research Funds for the Central Universities (Grant No. 2018B48614).

## References

- Akbari R, Hedayatzadeh R, Ziarati K, Hassanizadeh B (2012) A multi-objective artificial bee colony algorithm. *Swarm Evol Comput* 2(1): 39–52
- Alatas B, Akin E (2009) Multi-objective rule mining using a chaotic particle swarm optimization algorithm. *Knowl-Based Syst* 22(6): 455–460
- Alatas B, Akin E, Ozer AB (2009) Chaos embedded particle swarm optimization algorithm. *Chaos, Solitons Fractals* 40(4):1715–1734
- Bosman PAN, Thierens D (2003) The balance between proximity and diversity in multi-objective evolutionary algorithms. *IEEE Press* 7(2):174–188
- Briza AC, Naval Jr PC (2010) Stock trading system based on the multi-objective particle swarm optimization of technical indicators on end-of-day market data. *Appl Soft Comput* 11(1):1191–1201
- Coello CAC, Cortes NC (2002) An approach to solve multi-objective optimization problems based on an artificial immune system. *International Conference on Artificial Immune Systems*, 212–221
- Coello CAC, Lechuga MS (2002) MOPSO: a proposal for multiple objective particle swarm optimization. *Evolutionary Computation. CEC '02. Proceedings of the 2002 Congress on: 1051–1056*

- Coello CAC, Pulido GT, Lechuga MS (2004) Handling multiple objectives with particle swarm optimization. *IEEE Trans Evol Comput* 8(3):256–279
- Daynes S, Feih S, Lu WF, Wei J (2017) Optimisation of functionally graded lattice structures using isostatic lines. *Mater Des* 127:215–223
- Deb K, Pratap A, Agarwal S, Meyarivan T (2002) A fast and elitist multi-objective genetic algorithm: NSGA-II. *IEEE Trans Evol Comput* 6(2):182–197
- Eberhart RC, Shi YH (2002) Comparing inertial weights and constriction factor in particle swarm optimization. *Cong on Evolutionary Computation* 1(5):84–88
- Fantuzzi N, Tomabene F (2016) Strong formulation isogeometric analysis (SFIGA) for laminated composite arbitrary shaped plates. *Compos Part B* 96:173–203
- Farzam-Rad AS, Hassani B, Karamodin A (2017) Isogeometric analysis of functionally graded plates using a new quasi-3D shear deformation theory based on physical neutral surface. *Compos Part B* 108:174–189
- Hughes TJR, Cottrell JA, Bazilevs Y (2005) Isogeometric analysis: CAD, finite elements, NURBS, exact geometry and mesh refinement. *Comput Methods Appl Mech Eng* 194(39):4135–4195
- Kennedy J, Eberhart RC (1995) Particle swarm optimization. *IEEE Int Conf Neural Networks* 4:1942–1948
- Klinkel S, Chen L, Dornisch W (2015) A NURBS based hybrid collocation Galerkin method for the analysis of boundary represented solids. *Comput Methods Appl Mech Eng* 284:689–711
- Kou XY, Parks GT, Tan ST (2012) Optimal design of functionally graded materials using a procedural model and particle swarm optimization. *Comput Aided Des* 44(4):300–310
- Kulkarni NK, Patekar S, Bhoskar T, Kulkarni O, Kakandikar GM, Nandedkar VM (2015) Particle swarm optimization applications to mechanical engineering- a review. *Mater Today Proc* 2(4–5):2631–2639
- Lai WJ, Yu TT, Bui TQ, Wang ZG, Curiel-Sosa JL, Das R, Hirose S (2017) 3-D elasto-plastic large deformations: IGA simulation by Bézier extraction of NURBS. *Adv Eng Softw* 108:68–82
- Lezgy-Nazargah M, Vidal P, Polit O (2015) NURBS-based isogeometric analysis of laminated composite beams using refined sinus model. *Eur J Mech A Solids* 53:34–47
- Lieu QX, Lee J (2017) Modeling and optimization of functionally graded plates under thermo-mechanical load using isogeometric analysis and adaptive hybrid evolutionary firefly algorithm. *Compos Struct* 179:89–106
- Lieu QX, Lee J, Lee D, Lee S, Kim D, Lee J (2018) Shape and size optimization of functionally graded sandwich plates using isogeometric analysis and adaptive hybrid evolutionary firefly algorithm. *Thin-Walled Struct* 124:588–604
- Liew KM, Zhao X, Ferreira AJM (2011) A review of meshless methods for laminated and functionally graded plates and shells. *Compos Struct* 93(8):2031–2041
- Liu S, Yu TT, Bui TQ (2017a) Size effects of functionally graded micro-plates: a novel non-classical simple-FSDT isogeometric analysis. *Eur J Mech A Solids* 66:446–458
- Liu S, Yu TT, Bui TQ, Yin SH, Thai DK, Tanaka S (2017b) Analysis of functionally graded plates by a simple locking-free quasi-3D hyperbolic plate isogeometric method. *Compos Part B* 120:182–196
- Magnucka-Blandzi E (2011) Mathematical modelling of a rectangular sandwich plate with a metal foam core. *J Theor Appl Mech* 49(2):439–455
- Miettinen K (1999) *Nonlinear multi-objective optimization*. Kluwer Academic Publishers, New York
- Moita SJ, Araujo LA, Correia FV, Mota Soares MC, Herskovits J (2018) Material distribution and sizing optimization of functionally graded plate-shell structures. *Compos Part B* 142:263–272
- Na KS, Kim JH (2009) Volume fraction optimization of functionally graded composite panels for stress reduction and critical temperature. *Finite Elem Anal Des* 45(11):845–851
- Nair J, Howlin S, Porter J, Rimmer T (2006) Two-dimensional optimization of material composition of functionally graded materials using meshless analyses and a genetic algorithm. *Comput Methods Appl Mech Eng* 195(44):5926–5948
- Qasem SN, Shamsuddin SM (2011) Radial basis function network based on time variant multi-objective particle swarm optimization for medical diseases diagnosis. *Appl Soft Comput* 11(1):1427–1438
- Reddy JN (2004) *Mechanics of laminated composite plates and shells: theory and analysis*, 2nd edn. CRC Press
- Reissner E (1976) On the theory of transverse bending of elastic plates. *J Appl Mech* 12(8):545–554
- Roque CMC, Martins PALS, Ferreira AJM, Jorge RMN (2016) Differential evolution for free vibration optimization of functionally graded nano beams. *Compos Struct* 156:29–34
- Schaffer JD (1985) Multiple objective optimization with vector evaluated genetic algorithms. *International Conference on Genetic Algorithms*. L. Erlbaum Associates Inc, pp 93–100
- Schott JR (1995) Fault tolerant design using single and multicriteria genetic algorithm optimization. *Cell Immunol* 37(1):1–13
- Shi JX, Shimoda M (2015) Interface shape optimization of designing functionally graded sandwich structures. *Compos Struct* 125:88–95
- Singh N, Sinha A (2010) Chaos based multiple image encryption using multiple canonical transforms. *Opt Laser Technol* 42(5):724–731
- Srinivas N, Deb K (1994) Multiobjective optimization using nondominated sorting in genetic algorithms. *Evol Comput* 2(3):221–248
- Sun SH, Yu TT, Nguyen TT, Atroshchenko E, Bui TQ (2018) Structural shape optimization by IGABEM and particle swarm optimization algorithm. *Eng Anal Bound Elem* 88:26–40
- Svanberg K (1987) The method of moving asymptotes—a new method for structural optimization. *Int J Numer Methods Eng* 24(2):359–373
- Taheri AH, Hassani B (2014) Simultaneous isogeometrical shape and material design of functionally graded structures for optimal eigenfrequencies. *Comput Methods Appl Mech Eng* 277(2):46–80
- Taheri AH, Hassani B, Moghaddam NZ (2014) Thermo-elastic optimization of material distribution of functionally graded structures by an isogeometrical approach. *Int J Solids Struct* 51:416–429
- Tomabene F, Fantuzzi N, Bacciocchi M (2016) The GDQ method for the free vibration analysis of arbitrarily shaped laminated composite shells using a NURBS-based isogeometric approach. *Compos Struct* 154(1):190–218
- Vel SS, Batra RC (2002) Exact solution for thermoelastic deformations of functionally graded thick rectangular plates. *AIAA J* 40:1421–1433
- Vu TV, Nguyen NH, Khosravifard, Hematiyan MR, Tanaka S, Bui QT (2017) A simple FSDT-based meshfree method for analysis of functionally graded plates. *Eng Anal Bound Elem* 79:1–12
- Wang L, Xie NG, Song CZ, Bao JH, Cen YW (2010) Multi-objective bionics design method of passive suspension parameters based on hybrid behavior game. *Struct Multidiscip Optim* 42(3):371–386
- Wang L, Zhong X, Liu M (2012) A novel group search optimizer for multi-objective optimization. *Expert Syst Appl* 39(3):2939–2946
- Woodward B, Kashtalyan M (2011) 3D elasticity analysis of sandwich panels with graded core under distributed and concentrated loadings. *Int J Mech Sci* 53(10):872–885
- Xie NG, Meng R, Ye Y, Wang L, Cen YW (2013) Multi-objective design method based on evolution game and its application for suspension. *Struct Multidiscip Optim* 47(2):207–220
- Yin SH, Hale JS, Yu TT, Bui TQ, Bordas SPA (2014) Isogeometric locking-free plate element: a simple first order shear deformation theory for functionally graded plates. *Compos Struct* 118(1):121–138

- Yu TT, Yin SH, Bui TQ, Hirose S (2015) A simple FSDT-based isogeometric analysis for geometrically nonlinear analysis of functionally graded plates. *Finite Elem Anal Des* 96:1–10
- Yu TT, Bui TQ, Yin SH, Doan DH, Wu CT, Do TV, Tanaka S (2016a) On the thermal buckling analysis of functionally graded plates with internal defects using extended isogeometric analysis. *Compos Struct* 136:684–695
- Yu TT, Yin SH, Bui TQ, Xia SF, Tanaka S, Hirose S (2016b) NURBS-based isogeometric analysis of buckling and free vibration problems for laminated composites plates with complicated cutouts using a new simple FSDT theory and level set method. *Thin-Walled Struct* 101:141–156
- Yu TT, Yin SH, Bui TQ, Liu C, Wattanasakulpong N (2017) Buckling isogeometric analysis of functionally graded plates under combined thermal and mechanical loads. *Compos Struct* 162:54–69
- Zakaria MZ, Mohd Saad MS, Jamaluddin H, Ahmad R (2014) Dynamic system modeling of flexible beam system using multi-objective optimization differential evolution algorithm. *Appl Mech Mater* 695: 605–608
- Zaslavskii GM (1978) The simplest case of a strange attractor. *Phys Lett A* 69(3):145–147
- Zhu H, Sankar BV (2007) Analysis of sandwich TPS panel with functionally graded foam core by Galerkin method. *Compos Struct* 77(3):280–287
- Zitzler E, Thiele L (1999) Multi-objective evolutionary algorithms: a comparative case study and the strength Pareto approach. *IEEE Trans Evol Comput* 3(4):257–271

Accepted version